Letter

Viscosity ratio across interfaces controls the stability and self-assembly of microrollers

Blaise Delmotte *

LadHyX, CNRS, Ecole Polytechnique, Institut Polytechnique de Paris, 91120 Palaiseau, France

(Received 9 February 2023; accepted 25 May 2023; published 12 June 2023)

We investigate the individual and collective dynamics of torque-driven particles, called microrollers, near fluid-fluid interfaces. We find that the viscosity ratio across the interface controls the speed and direction of the particles, their relative motion, the growth of a fingering instability, and the self-assembled motile structures that emerge from it. By combining theory and large scale numerical simulations, we show how the viscosity ratio across the interface governs the long-range hydrodynamic interactions between particles and thus their collective behavior.

DOI: 10.1103/PhysRevFluids.8.L062302

The motion of small driven particles near interfaces is observed in numerous biological and artificial systems [1–3]. Examples include droplets filled with self-propelled particles, where hydrodynamic couplings between the particles and the surrounding fluid-fluid interface induce collective motion and translation of the droplet [4–9]. Navigation near interfaces also happens in natural environments with air-water interfaces, such as marine foams [10] or films [11–13], and in biomedical environments where microswimmers move near soft vessel walls, viscoelastic media (biofilms, gels, tissues), or mucus layers [14–16].

Among them, spinning particles, such as torque-driven colloids (also called microrollers), use rotation-translation couplings near surfaces to self-propel. Synthetic microrollers are actuated by an external magnetic field rotating about an axis parallel to the interface. The orientation of the magnetic field can be varied over time to guide these particles in a variety of environments. Thanks to their steerability and to the strong long-range flows they generate, they offer promising perspectives for particle micromanipulation, fluid pumping, and drug delivery in microfluidic and biological systems [17–24]. Above a rigid wall, hydrodynamic interactions between microrollers induce a variety of collective motions such as periodic leapfrog orbits [25,26], the formation of fast moving layers [27–29], the emergence of dense fronts [30], and the growth of a fingering instability that releases stable motile clusters [31–33]. However, despite the rich and well documented dynamics observed above rigid boundaries, little is known about their collective behavior near interfaces.

In this Letter, we combine theory and simulations to investigate the dynamics of microrollers near fluid-fluid interfaces. We show how the viscosity ratio across the interface, denoted ξ, modifies the flow around the spinning particles, with amazing consequences on their individual and collective motion. At the individual level, we find that ξ controls the direction and speed of a single microroller. At the pair level, ξ acts as an order parameter on their relative motion that determines the existence of periodic orbits. At the collective level, ξ controls both the growth rate of the fingering instability initially observed above a no-slip surface, and the self-assembly process that leads to the emergence of motile clusters. As discussed in the conclusions, the ability to control the macroscopic response of these active suspensions opens promising perspectives for microfluidics applications.

*blaise.delmotte@cnrs.fr

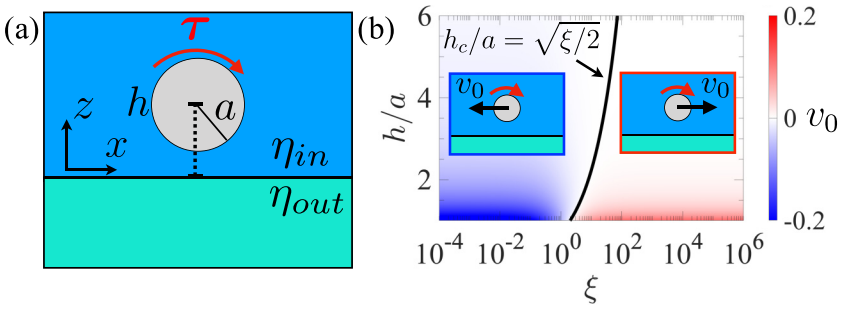

FIG. 1. (a) Schematic of a torque-driven particle above a fluid-fluid interface. (b) Self-induced velocity of the particle v_0 in response to a constant torque τ as a function of $\xi = \eta_{\text{out}}/\eta_{\text{in}}$ and normalized height h/a.

We consider the motion of small torque-driven spherical particles with radius a suspended in a fluid with dynamic viscosity η_{in} above a fluid-fluid interface [Fig. 1(a)]. The outer fluid on the other side of the interface has dynamic viscosity η_{out} which can vary from zero (e.g., air) to $+\infty$ (a rigid wall). We denote $\xi = \eta_{\text{out}}/\eta_{\text{in}}$ the viscosity ratio between the two fluids across the interface. In this work we consider particles with large contact angles that are not adsorbed to the surface (such as paramagnetic beads above air/water surfaces [27]). In typical experiments the particles are micron-sized [$a = O(1)\mu$m] and suspended in water ($\eta_{\text{in}} = 10^{-3}$ Pa s). They rotate in synchrony with an external magnetic field with frequency $f = O(10)$Hz thanks to a magnetic torque aligned with the y axis denoted τ. The corresponding capillary number is $\text{Ca} = \eta_{\text{in}} u/\gamma \approx 10^{-6}$–$10^{-5}$, where $u = \omega a = 2\pi f a$ is the maximal fluid velocity, reached on the particle surface due to the no-slip condition, and $\gamma = O(10^{-2})$N/m is the typical surface tension between the two phases. Owing to the very small value of Ca and to the small size of the particles, the interface can be approximated as flat and nondeformable for all values of ξ [34]. In this limit, one can compute the flow field around the particles using the Green's function $\boldsymbol{G}$ of the Stokes equations which, by linearity, is given by [35]

$$\boldsymbol{G} = 1/(\xi+1)\boldsymbol{G}^{FS} + \xi/(\xi+1)\boldsymbol{G}^{W}, \tag{1}$$

where $\boldsymbol{G}^{FS}$ is the Green's function of a domain bounded by a flat free surface and $\boldsymbol{G}^{W}$ a domain bounded by a flat no-slip wall, both of which have known analytical expressions based on image systems [34,36].[1] Changing ξ from 0 to $+\infty$ in Eq. (1) transitions smoothly from a free surface to a no-slip wall.

Single particle motion. Using the Faxen formulas for the motion of a spherical particle in a nonuniform flow [38], the far-field approximation of the self-induced velocity of a single microroller above the interface, is given by, see Supplemental Material [39],

$$v_0(\xi, h/a) = \frac{1}{4}\left(\frac{a}{h}\right)^2\left[-\frac{1}{\xi+1} + \frac{\xi}{\xi+1}\frac{1}{2}\left(\frac{a}{h}\right)^2\right], \tag{2}$$

where the velocity has been normalized by $\tau/8\pi\eta a^2$. Interestingly, the sign of the velocity in Eq. (2) depends both on the viscosity ratio *and* the particle height [Fig. 1(b)]. Below a critical value $\xi_c = 2$ the velocity is always negative, even though the applied torque is clockwise, and decays as $(a/h)^2$ for $\xi = 0$. This surprising backward motion has already been observed experimentally [27] and is due to the fact there is no velocity gradient on the free-surface underneath. The particle therefore experiences more viscous stress on its upper side, where velocity gradients are larger, than on the lower side. As a result, the particle "rolls" on the liquid above, which resists more against rotational motion, and thus moves backwards. When $\xi \geqslant \xi_c$, there is a critical height $h_c = \sqrt{\xi/2}a$

[1] Note that if the interface is not flat, e.g., near a small droplet, Eq. (1) involves additional terms that cannot be written as simple linear combinations of $\boldsymbol{G}^{FS}$ and $\boldsymbol{G}^{W}$ [37].

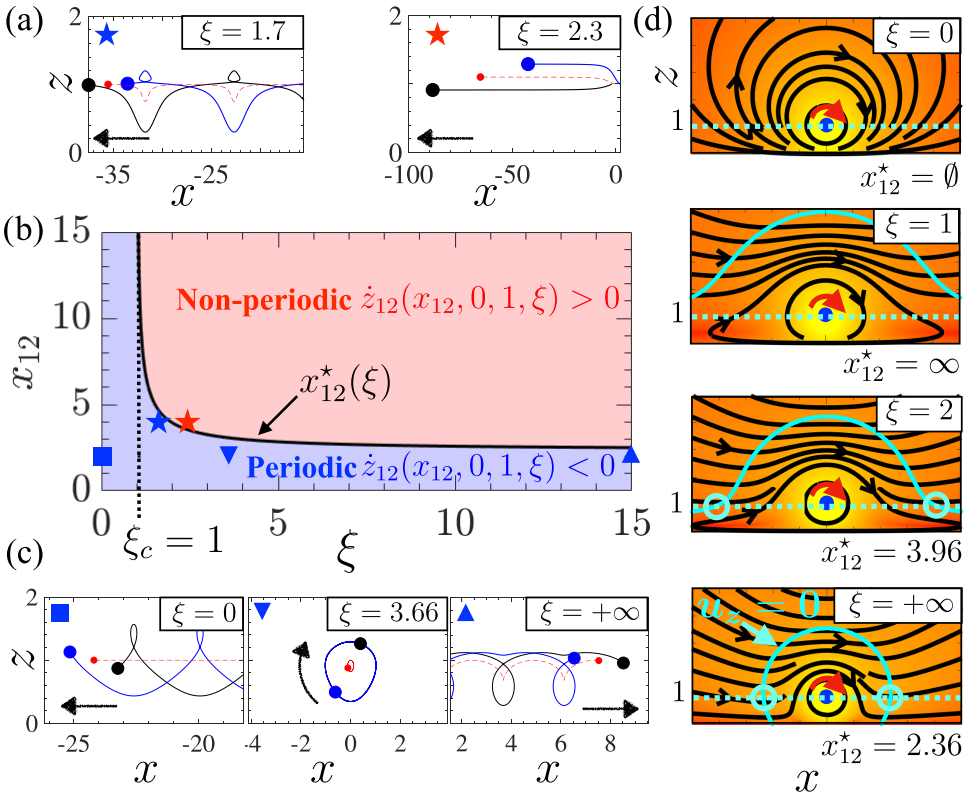

FIG. 2. (a) Effect of ξ on the periodicity of trajectories of two rotlets (blue and black disks) with identical initial separation: $x^0_{12} = 4$. Red disk and dashed line: position and trajectory of the center of mass (x_C, z_C). Black arrow: direction of motion of x_C. (b) Phase diagram of rotlet orbits near the critical points as a function of ξ and x_{12}. Black line: critical distance $x^\star_{12}$. (c) Effect of ξ on the direction of motion of a pair with $x^0_{12} = 2$. (d) Streamlines and flow field around a rotlet in the (x, z) plane for various ξ. Cyan solid line: isovalue $u_z = 0$. Cyan dotted line: $z = 1$. Cyan circles: position of the critical horizontal separation $x^\star_{12}$, reported below each panel.

at which viscous stresses balance between both sides such that the particle rotates in place, i.e., $v_0(\xi > \xi_c, h_c) = 0$. v_0 is positive below h_c and negative above. In the limit of a no-slip wall, $\xi \to +\infty$, v_0 is always positive and decays as $(a/h)^4$. These results show that both the direction and speed of a rotating particle can be controlled with the viscosity ratio.

Pair dynamics. When adding another particle in the system, the trajectories exhibit a richer dynamics than the individual motion described above: particles can follow a variety of periodic orbits, change direction or end up translating at a steady speed [Figs. 2(a)–2(c)]. We consider two torque-driven particles, lying in the (x, z) plane vertical to the floor and separated by a distance $r_{12} = \sqrt{x_{12}^2 + z_{12}^2}$, where $x_{12} = x_1 - x_2$ and $z_{12} = z_1 - z_2$. For simplicity, we focus on the limit $a \ll \min(r_{12}, z_1, z_2)$, where the particles are considered as point-torques (rotlets) so that the equations of motion can be written compactly as a simple dynamical system with three degrees of freedom [39]:

$$\begin{bmatrix} \dot{x}_{12} \\ \dot{z}_{12} \\ \dot{z}_C \end{bmatrix} = \begin{bmatrix} 2z_{12}\left(\frac{1}{r_{12}^3} - \frac{\xi}{\xi+1}\frac{2x_{12}^2 - 4z_C^2}{R_{12}^5}\right) + \delta v_0 \\ 2x_{12}\left(\frac{1}{R_{12}^3} - \frac{1}{r_{12}^3} + \frac{\xi}{\xi+1}\frac{12z_C^2}{R_{12}^5}\right) \\ \frac{\xi}{\xi+1}\frac{6x_{12}z_{12}z_C}{R_{12}^5} \end{bmatrix}, \tag{3}$$

where $z_C = (z_1 + z_2)/2$, and $R_{12} = \sqrt{x_{12}^2 + 4z_C^2}$. $\delta v_0 = -\frac{1}{4}\frac{1}{\xi+1}((z_C + z_{12}/2)^{-2} - (z_C - z_{12}/2)^{-2})$ is the difference between the self-induced velocities in the point-particle limit. Here, lengths have been rescaled by the initial height of the system $l_c = z_C^0 = z_C(t = 0)$ and time by $t_c = 8\pi\eta l_c^3/\tau$. The dynamical system (3) has two critical saddle points with coordinates $\boldsymbol{x}_\pm^\star = (x_{12} = \pm x_{12}^\star, z_{12} = 0, z_C = 1)$, where $x_{12}^\star \neq 0$ is a zero of $\dot{z}_{12}(x_{12}, 0, 1, \xi)$ [39]. These critical points separate periodic (leapfrog) and nonperiodic orbits, as shown in Fig. 2(b). Interestingly, their position, $x_{12}^\star$, is controlled by the viscosity ratio ξ. To visualize this dependency, we examine the changes in the topology of the flow field around a spinning particle as a function of ξ [Fig. 2(d)]. When $\xi = 0$ all the streamlines in the domain are closed and circular. As ξ increases, the region of closed streamlines contracts in the vicinity of the particle, while open streamlines, which push the fluid forward, occupy more space. To understand the effect of the flow on the periodicity of the orbits we place the particles at the critical point $x_{12} = x_{12}^\star$, where $z_1 = z_2 = 1$ and we assume $x_1 > x_2$. At this position their relative, and thus absolute, vertical velocity vanishes $\dot{z}_{12} = 0 \Rightarrow \dot{z}_1 = \dot{z}_2 = \dot{z}_C = 0$. $x_{12}^\star$ therefore corresponds to the intersection between the contour of zero vertical fluid velocity induced by a particle, $u_z = 0$, and the line $z = 1$ as shown on Fig. 2(d). If $x_{12} > x_{12}^\star$ then $\dot{z}_{12} > 0$ and the particles cannot perform the leapfrog motion, as can be intuited by superimposing the flow of two rotlets side by side [Figs. 2(a) and 2(d)]. Below a critical value $\xi_c = 1$, $\dot{z}_{12}$ is always negative at $z = 1$, which implies that there is no critical point $x_{12}^\star$ ($u_z = 0$ and $z = 1$ never meet) and thus that all the trajectories are periodic regardless of the initial separation [Figs. 2(b)–2(d)]. The viscosity ratio therefore controls the existence of periodic orbits. The viscosity ratio also sets the speed and direction of these periodic motions. In the limit $\xi = 0$ the backward motion is fastest and the height of the system remains constant ($\dot{z}_C = 0$) [Fig. 2(c), left panel]. Otherwise the direction of motion depends on the relative position of the particles so that, given an initial configuration, there is always a threshold value for which the pair orbits in place [e.g., $\xi = 3.66$ for $x_{12}^0 = 4$ in Fig. 2(c), middle panel]. In the limit $\xi = +\infty$, the pair always moves forward: $\dot{x}_C = 6z_C x_{12}^2/R_{12}^5 > 0$ [Fig. 2(c), right panel].

Collective dynamics. We further explore the dynamics at the collective level where large collections of particles interact. In the rigid-wall limit ($\xi \to \infty$) the suspension exhibits a cascade of events: an initially uniform strip of particles forms a dense front which is subject to a transverse fingering instability, from which the fingertips then detach to generate dense motile structures. As shown in previous work, the wavelength at the onset of the instability is set by the mean height of the front [31,32]. We investigate the effect of the viscosity ratio on this rich collective dynamics using three-dimensional Stokesian dynamics simulations that include both hydrodynamic and steric interactions between tens of thousands of microrollers above the interface [39]. Figure 3 a shows the time evolution of 10^4 microrollers initially lying on a monolayer with area fraction $\phi = 0.65$, at a given height $z_C^0/a = 1.2$, for various viscosity ratios $\xi \in \{0, 0.5, 1.5, 5, +\infty\}$ (see Supplemental Material Movies 1–2). In the case of a no-slip wall, $\xi = +\infty$, the strips evolves as described above. The rollers inside the fingertips perform a treadmill motion that follows the clockwise rotation of the torque. A few particles are occasionally shed from the front and lifted up by flow of the rotating structures. When $\xi = 5$ the suspension behaves similarly with a slower forward motion. At a critical value $\xi \approx 1.5$, the suspension treadmills without translating, but the transverse instability still occurs in place, leading to a lateral separation of the particles. Below that threshold, the suspension self-assembles into a long roll treadmilling clockwise but moving backwards. When $\xi = 0.5$ the roll is wavy due to the transverse instability, but evolves at a significantly slower rate, and sporadically sheds particles from the rear. In the free-surface limit ($\xi = 0$), the transverse instability is suppressed and the roll remains straight and stable. It does not shed any particle because, as shown in the previous section, the streamlines of the flow induced by the microrollers are closed regardless of the separation distance [Fig. 2(b), bottom panel]. Finally, we note that the mean height of the particles in the fingertips slightly increases with ξ [Fig. 3(a), bottom panel], which in turn increases the wavelength of the transverse instability. This is due to the upward advective flows ahead of the

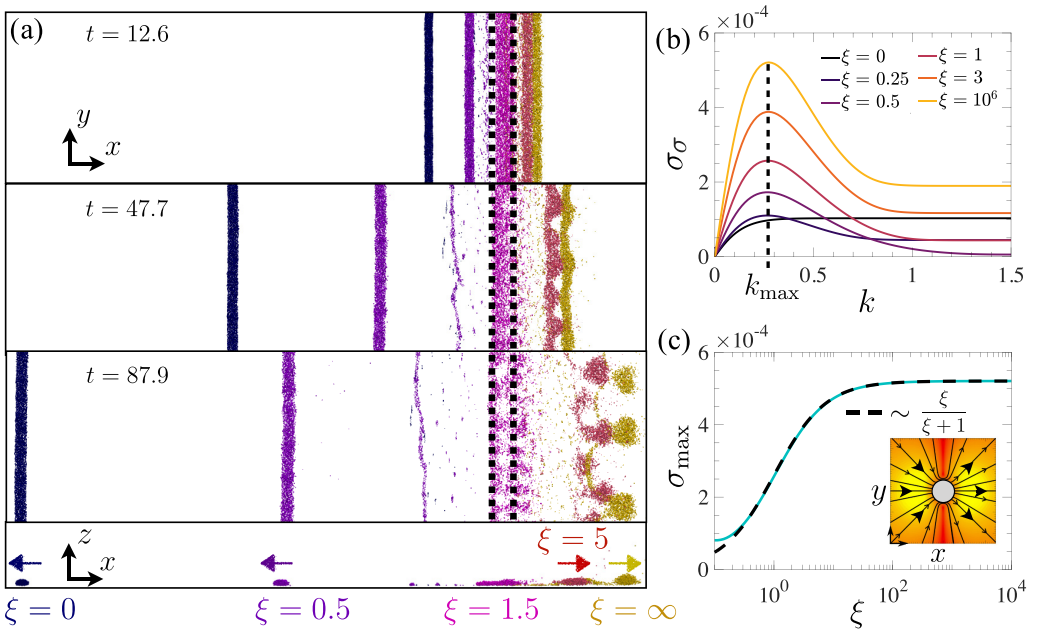

FIG. 3. (a) Time-evolution of 10,000 microrollers initially uniformly distributed in a monolayer (delimited by the black dotted lines) above the interface. Each color corresponds to a different value of $\xi \in \{0, 0.5, 1.5, 5, +\infty\}$ simulated independently. Bottom panel: side view at $t = 87.9$. Arrows: direction of motion. (b) Growth rate of the two line model Eqs. (4)–(5) for various ξ. Dashed line: fastest growing mode $k_{\max}$. (c) Maximum growth rate (solid cyan line) as a function of ξ. Dashed black line: prefactor $\sim \xi/(\xi + 1)$ due to the transverse flows generated above a no-slip boundary (inset).

particles that get stronger with ξ [see Fig. 2(b)] and allow the particles behind to lift the leading front where the instability occurs.

In order to better understand the effect of ξ on the transverse instability, we use a simple model consisting of two continuous lines of rotlets separated by a distance d in a plane parallel to the interface at a constant height h. The lines are aligned along the y axis with rotlet density $\rho_i(y, t)$ and position $x_i(y, t)$, $i = 1, 2$. The model is governed by the equations of motion of each line together with the conservation of rotlets along their length:

$$\begin{aligned} \frac{\partial x_i(y,t)}{\partial t} &= u_x(x_i(y,t), y) \\ \frac{\partial \rho_i(y,t)}{\partial t} &= -\frac{\partial [\rho_i(y,t) u_y(x_i(y,t), y)]}{\partial y}, \end{aligned} \quad i = 1, 2, \tag{4}$$

where length and time have been rescaled with $l_c = h$ and t_c defined above. The velocity (u_x, u_y) in the right-hand side arises from the long-ranged hydrodynamic interactions between the microrollers of each line, e.g.,

$$u_x(\underbrace{x_i, y}_{\boldsymbol{x}}) = \sum_{j=1}^{2} \int_{-\infty}^{+\infty} \mu_x^{u\tau}(\underbrace{x_i - x_j, y - y'}_{\boldsymbol{x}-\boldsymbol{x}'}) \rho_j(y') \mathrm{d}y', \tag{5}$$

where $\mu_x^{u\tau}(\boldsymbol{x} - \boldsymbol{x}')$ is the x component of the operator $\boldsymbol{\mu}^{u\tau}(\boldsymbol{x} - \boldsymbol{x}') = 1/2(\nabla_{\boldsymbol{x}'} \times \boldsymbol{G}(\boldsymbol{x} - \boldsymbol{x}')) \cdot \boldsymbol{e}_y$ that computes the fluid velocity at position $\boldsymbol{x}$ induced by a rotlet, directed along $\boldsymbol{e}_y$, at position $\boldsymbol{x}'$ [39]. As shown in previous work, this model contains all the essential ingredients to faithfully reproduce the fingering instability above a no-slip wall [31] and naturally extends to fluid-fluid interfaces by using

the linear combination of Green's functions in Eq. (1). The base state of this system corresponds to two straight lines with uniform rotlet densities $[\rho_i(y,t) = \rho_0]$ translating at a steady speed, so that their position are constant in the moving frame ($x_1(y,t) = 0$, $x_2(y,t) = d$). After carrying a linear stability analysis of the system around the base state, we obtain an analytical expression for the growth rate $\sigma(k,\xi)$ [39], plotted in Fig. 3(b). First, we notice that an identical fastest growing mode is selected for all values of ξ, as seen by the clear bump at $\lambda_{\max} = 2\pi/k_{\max} = 23$, except for $\xi = 0$ for which there is no clear selection. The existence of a plateau at large k is specific to the two-lines model, and its dependence on ξ is explained in the Supplemental Material [39]. Second the corresponding growth rate, $\sigma_{\max}$, increases with ξ. The increase of $\sigma_{\max}$ is quantified on Fig. 3(c), and shows a plateau at large ξ. A detailed analysis of the two-line model shows that the growth rate of the transverse instability is proportional to the transverse flow u_y in Eq. (4). Since the microrollers do not induce transverse flows above a free surface ($u_y^{FS} = 0$ [39]), $\sigma_{\max}$ scales as $\xi/(\xi+1)$, which is the prefactor of the no-slip wall contribution $\boldsymbol{G}^W$ in Eq. (1) [see inset of Fig. 3(c)]. Overall the two-line model highlights the crucial role of these transverse flows and exhibits a good agreement with the simulations in the sense that, for a given particle height, ξ only changes the growth rate of the instability without affecting much the dominant wavelength. However since the height of the particles is kept constant in the model, it cannot capture the slight increase of the wavelength with ξ that is observed on Fig. 3(a).

The nature of the interface does not only affect the direction of motion of the suspension and the growth of the transverse instability, but also the shape and structure of the emerging clusters. We study these changes from a macroscopic point of view, with a mean field description of the density of microrollers $\rho(\boldsymbol{x},t)$ in the (x,z) plane perpendicular to the interface, denoted $\mathcal{P}$. $\rho(\boldsymbol{x},t)$ obeys a conservation equation

$$\frac{\partial \rho}{\partial t} + \nabla \cdot (\boldsymbol{u}\rho) = 0. \tag{6}$$

The velocities in the flux term arise from the long-ranged hydrodynamic interactions between microrollers in the plane $\mathcal{P}$, e.g., $u_x(\boldsymbol{x},t) = \int_{\mathcal{P}} \mu_x^{u\tau}(\boldsymbol{x}-\boldsymbol{x}')\rho(\boldsymbol{x}',t)\mathrm{d}\boldsymbol{x}'$. The nonlocal equation (6) is solved numerically [39–41] and the rollers are initially uniformly distributed ($\rho = \rho_0$) over a thin strip of aspect ratio $\Gamma = L/H = 9.4$ near the interface. After some time, the system reaches a quasisteady state where a main cluster emerges and translates at a steady speed (see Supplemental Material Movies 3–7). Figure 4 shows a snapshot of the microroller density at the same dimensionless time in the quasipermanent regime for various values of ξ together with the density $\rho(x_C,z)$ and velocity profiles $u_x(x_C,z)$ at the central cross section of the cluster. The cluster is delimited by the isovalue $\rho = 0.4\rho_0$ (red line). As in the discrete particle simulations, the velocity of the cluster is fastest and backwards for $\xi = 0$, vanishes around $\xi \approx 1.1$, where the cluster treadmills in place, and increases forward beyond. The shape of the cluster evolves from a near-hemisphere of aspect ratio $\Gamma = 3.1$ at $\xi = 0$, to a "pancake" shape ($\Gamma = 8.4$) at $\xi = 1.1$, and becomes circular when ξ increases further ($\Gamma = 2$ and $\Gamma = 1.4$ for $\xi = 5$ and $\xi = +\infty$). In addition to the shape, ξ controls the particle distribution inside the cluster. The distribution is uniform at $\xi = 0$ ($\rho \approx \rho_0$) and becomes more peaked as ξ increases, with a maximum $\rho_{\max} \approx 3.8\rho_0$ reached at $\xi = +\infty$. These changes in concentration, together with the boundary condition at the interface underneath, determine the velocity profile within the cluster. At $\xi = 0$, the treadmilling motion is fastest near the bottom interface, where the slip condition allows for large velocities. As ξ increases, the particles concentrate at the center and the no-slip condition becomes stronger, which shifts the maximum velocity upwards and generates a rigid-body motion near the core.

Discussion. In this Letter, we have shown that the viscosity ratio across interfaces controls both the microscopic and macroscopic response of an active suspension. These fundamental findings are also of technological importance. Our results suggest that the strategies for particle transport and fluid pumping initially developed with microrollers above solid walls can readily be extended to a variety of biological and microfluidic environments with different type of surfaces. Our results could even generalize to solid boundaries with a finite slip length [42], which are found in many

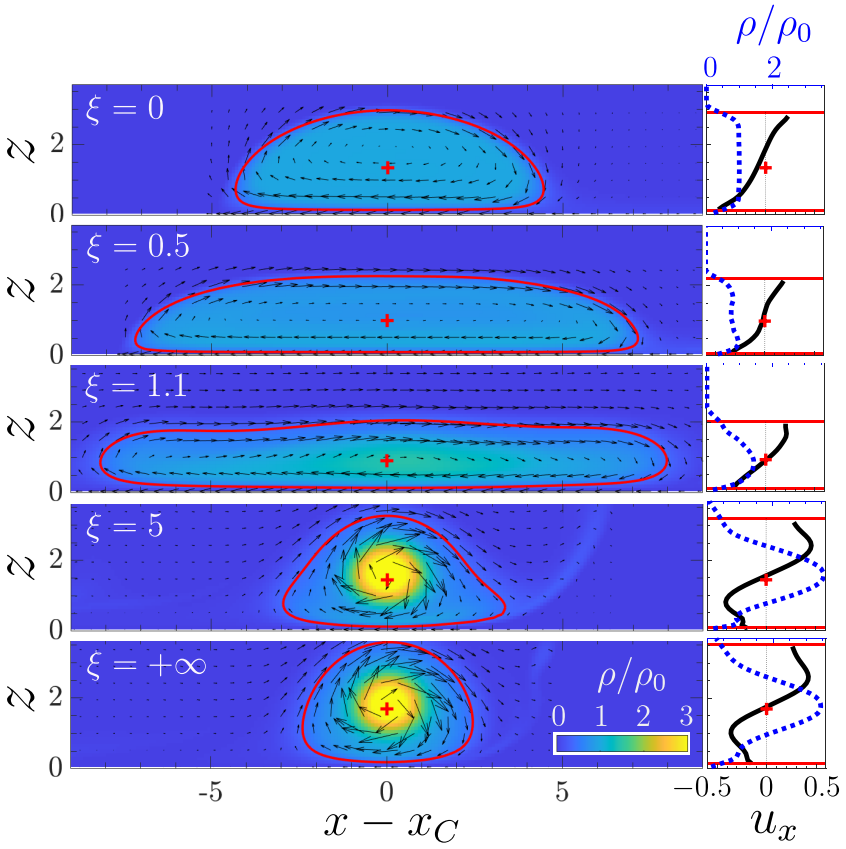

FIG. 4. Particle density distribution $\rho(\boldsymbol{x}, t)$ obtained from (6) at $t = 1418$ (quasisteady state) in the (x, z) plane for various $\xi \in \{0, 0.5, 1.5, 5, +\infty\}$. Black arrows: flow field. Solid red line: $\rho/\rho_0 = 0.4$. Red cross: position of the center of mass (x_C, z_C). Side panels: density (dotted blue line) and velocity (solid black line) profiles at $x = x_C$.

experimental systems, such as hydrophobic surfaces. In this work we considered particles lying *above* the interface, i.e., with large contact angles. In some cases the particles wet the outer fluid and get adsorbed at the interface. Adsorbed active particle layers can be used as active surfactants to modulate interfacial properties in emulsions or films, or to pump and mix flows in the surrounding fluids [3,43]. Up to now, the hydrodynamics of torque-driven particles straddling fluid-fluid interfaces is still not well understood [44] and should deserve more attention given their exciting applications.

I thank M. Driscoll, A. Donev, and S. Michelin for their critical reading of the manuscript as well as for stimulating discussions. I acknowledge support from the French National Research Agency (ANR), under award no. ANR-20-CE30-0006. I also thank the NVIDIA Academic Partnership program for providing GPU hardware for performing some of the simulations reported here.

[1] E. Lauga, Bacterial hydrodynamics, Annu. Rev. Fluid Mech. **48**, 105 (2016).

[2] C. Bechinger, R. Di Leonardo, H. Löwen, C. Reichhardt, G. Volpe, and G. Volpe, Active particles in complex and crowded environments, Rev. Mod. Phys. **88**, 045006 (2016).

[3] W. Fei, Y. Gu, and K. J. Bishop, Active colloidal particles at fluid-fluid interfaces, Curr. Opin. Colloid Interface Sci. **32**, 57 (2017).
[4] T. Gao and Z. Li, Self-Driven Droplet Powered By Active Nematics, Phys. Rev. Lett. **119**, 108002 (2017).
[5] B. Vincenti, G. Ramos, M. L. Cordero, C. Douarche, R. Soto, and E. Clement, Magnetotactic bacteria in a droplet self-assemble into a rotary motor, Nat. Commun. **10**, 5082 (2019).
[6] D. P. Singh, A. Domínguez, U. Choudhury, S. N. Kottapalli, M. N. Popescu, S. Dietrich, and P. Fischer, Interface-mediated spontaneous symmetry breaking and mutual communication between drops containing chemically active particles, Nat. Commun. **11**, 2210 (2020).
[7] Z. Huang, T. Omori, and T. Ishikawa, Active droplet driven by a collective motion of enclosed microswimmers, Phys. Rev. E **102**, 022603 (2020).
[8] M. Rajabi, H. Baza, T. Turiv, and O. D. Lavrentovich, Directional self-locomotion of active droplets enabled by nematic environment, Nat. Phys. **17**, 260 (2021).
[9] G. Kokot, H. A. Faizi, G. E. Pradillo, A. Snezhko, and P. M. Vlahovska, Spontaneous self-propulsion and nonequilibrium shape fluctuations of a droplet enclosing active particles, Commun. Phys. **5**, 91 (2022).
[10] Q. Roveillo, J. Dervaux, Y. Wang, F. Rouyer, D. Zanchi, L. Seuront, and F. Elias, Trapping of swimming microalgae in foam, J. R. Soc. Interface. **17**, 20200077 (2020).
[11] R. Di Leonardo, D. Dell'Arciprete, L. Angelani, and V. Iebba, Swimming with an Image, Phys. Rev. Lett. **106**, 038101 (2011).
[12] M. Morse, A. Huang, G. Li, M. R. Maxey, and J. X. Tang, Molecular adsorption steers bacterial swimming at the air/water interface, Biophys. J. **105**, 21 (2013).
[13] A. J. Mathijssen, A. Doostmohammadi, J. M. Yeomans, and T. N. Shendruk, Hotspots of boundary accumulation: Dynamics and statistics of micro-swimmers in flowing films, J. R. Soc. Interface. **13**, 20150936 (2016).
[14] S. S. Suarez and A. Pacey, Sperm transport in the female reproductive tract, Human Reproduction Update **12**, 23 (2006).
[15] D. Lopez and E. Lauga, Dynamics of swimming bacteria at complex interfaces, Phys. Fluids **26**, 071902 (2014).
[16] Y. Alapan, U. Bozuyuk, P. Erkoc, A. C. Karacakol, and M. Sitti, Multifunctional surface microrollers for targeted cargo delivery in physiological blood flow, Sci. Robot. **5**, eaba5726 (2020).
[17] B. Kavčič, D. Babič, N. Osterman, B. Podobnik, and I. Poberaj, Magnetically actuated microrotors with individual pumping speed and direction control, Appl. Phys. Lett. **95**, 023504 (2009).
[18] F. Martinez-Pedrero and P. Tierno, Magnetic Propulsion of Self-Assembled Colloidal Carpets: Efficient Cargo Transport Via a Conveyor-Belt Effect, Phys. Rev. Appl. **3**, 051003 (2015).
[19] F. Martínez-Pedrero and P. Tierno, Advances in colloidal manipulation and transport via hydrodynamic interactions, J. Colloid Interface Sci. **519**, 296 (2018).
[20] M. Driscoll and B. Delmotte, Leveraging collective effects in externally driven colloidal suspensions: Experiments and simulations, Curr. Opin. Colloid Interface Sci. **40**, 42 (2019).
[21] A. Chamolly, E. Lauga, and S. Tottori, Irreversible hydrodynamic trapping by surface rollers, Soft Matter **16**, 2611 (2020).
[22] X. Qi, S. Wang, S. Ma, K. Han, X. Bian, and X. Li, Quantitative prediction of rolling dynamics of leukocyte-inspired microroller in blood flow, Phys. Fluids **33**, 121908 (2021).
[23] U. Bozuyuk, E. Suadiye, A. Aghakhani, N. O. Dogan, J. Lazovic, M. E. Tiryaki, M. Schneider, A. C. Karacakol, S. O. Demir, G. Richter *et al.*, High-performance magnetic FePt ($L1_0$) surface microrollers towards medical imaging-guided endovascular delivery applications, Adv. Funct. Mater. **32**, 2109741 (2022).
[24] A. F. Demirörs, A. Stauffer, C. Lauener, J. Cossu, S. N. Ramakrishna, J. De Graaf, C. C. Alcantara, S. Pané, N. Spencer, and A. R. Studart, Magnetic propulsion of colloidal microrollers controlled by electrically modulated friction, Soft Matter **17**, 1037 (2021).
[25] F. Martinez-Pedrero, E. Navarro-Argemí, A. Ortiz-Ambriz, I. Pagonabarraga, and P. Tierno, Emergent hydrodynamic bound states between magnetically powered micropropellers, Sci. Adv. **4**, eaap9379 (2018).

[26] B. Delmotte, Hydrodynamically bound states of a pair of microrollers: A dynamical system insight, Phys. Rev. Fluids **4**, 044302 (2019).
[27] F. Martinez-Pedrero, A. Ortiz-Ambriz, I. Pagonabarraga, and P. Tierno, Colloidal Microworms Propelling via a Cooperative Hydrodynamic Conveyor Belt, Phys. Rev. Lett. **115**, 138301 (2015).
[28] B. Sprinkle, E. B. Van Der Wee, Y. Luo, M. M. Driscoll, and A. Donev, Driven dynamics in dense suspensions of microrollers, Soft Matter **16**, 7982 (2020).
[29] G. Junot, A. Cebers, and P. Tierno, Collective hydrodynamic transport of magnetic microrollers, Soft Matter **17**, 8605 (2021).
[30] B. Delmotte, M. Driscoll, P. Chaikin, and A. Donev, Hydrodynamic shocks in microroller suspensions, Phys. Rev. Fluids **2**, 092301(R) (2017).
[31] B. Delmotte, A. Donev, M. Driscoll, and P. Chaikin, Minimal model for a hydrodynamic fingering instability in microroller suspensions, Phys. Rev. Fluids **2**, 114301 (2017).
[32] M. Driscoll, B. Delmotte, M. Youssef, S. Sacanna, A. Donev, and P. Chaikin, Unstable fronts and motile structures formed by microrollers, Nature Phys. **13**, 375 (2017).
[33] F. B. Usabiaga, B. Delmotte, and A. Donev, Brownian dynamics of confined suspensions of active microrollers, J. Chem. Phys. **146**, 134104 (2017), software available at https://github.com/stochasticHydroTools/RigidMultiblobsWall.
[34] S. Lee, R. Chadwick, and L. G. Leal, Motion of a sphere in the presence of a plane interface. Part 1. An approximate solution by generalization of the method of Lorentz, J. Fluid Mech. **93**, 705 (1979).
[35] J. W. Swan and J. F. Brady, Simulation of hydrodynamically interacting particles near a no-slip boundary, Phys. Fluids **19**, 113306 (2007).
[36] J. Blake and A. Chwang, Fundamental singularities of viscous flow, J. Eng. Math. **8**, 23 (1974).
[37] Y. O. Fuentes, S. Kim, and D. J. Jeffrey, Mobility functions for two unequal viscous drops in Stokes flow. II. Asymmetric motions, Phys. Fluids **1**, 61 (1989).
[38] S. Kim and S. J. Karrila, *Microhydrodynamics: Principles and Selected Applications* (Butterworth-Heinemann, Boston, 1991).
[39] See Supplemental Material at http://link.aps.org/supplemental/10.1103/PhysRevFluids.8.L062302 for supplemental notes, details on numerical simulations, and movies.
[40] J. B. Bell, C. N. Dawson, and G. R. Shubin, An unsplit, higher order Godunov method for scalar conservation laws in multiple dimensions, J. Comput. Phys. **74**, 1 (1988).
[41] S. May, A. Nonaka, A. Almgren, and J. Bell, An unsplit, higher-order Godunov method using quadratic reconstruction for advection in two dimensions, Communications in Applied Mathematics and Computational Science **6**, 27 (2011).
[42] E. Lauga and T. M. Squires, Brownian motion near a partial-slip boundary: A local probe of the no-slip condition, Phys. Fluids **17**, 103102 (2005).
[43] W. Fei, P. M. Tzelios, and K. J. M. Bishop, Magneto-capillary particle dynamics at curved interfaces: Time-varying fields and drop mixing, Langmuir **36**, 6859 (2020).
[44] C. Maldarelli, N. T. Donovan, S. C. Ganesh, S. Das, and J. Koplik, Continuum and molecular dynamics studies of the hydrodynamics of colloids straddling a fluid interface, Annu. Rev. Fluid Mech. **54**, 495 (2022).